13B.5   IMPACT OF MICROPHYSICS PARAMETERIZATIONS ON SIMULATION OF 13 MARCH 2003 BOW ECHO

Rebecca D. Adams-Selin[1,2*], Richard H. Johnson[2], and Susan C. van den Heever[2]

[1]Atmospheric and Environmental Research, Inc.,
Lexington, Massachusetts

[2]Department of Atmospheric Science,
Colorado State University, Fort Collins, Colorado

1. INTRODUCTION

It is well known that a key component to the strength, structure, and longevity of squall lines and bow echoes is the cold pool (Weisman et al. 1992; Weisman et al. 1993). Changes in the rates of cooling by microphysical processes naturally have a large effect on the shape and strength of the cold pool, and hence the eventual storm structure and development. While the impact of microphysics scheme variations on cold pool and storm structure have been noted for supercells (Gilmore et al. 2004, van den Heever and Cotton 2004, Snook and Xue 2006, Dawson et al. 2007, Dawson et al. 2008), few studies have looked at the effects on mesoscale convective systems, specifically squall lines and bow echoes.

The microphysical processes in a squall line trailing stratiform region were diagnosed by Gallus and Johnson (1995) using a two-dimensional model. At initiation, cooling by melting and evaporation took place just behind the convective line, resulting in a cold pool with a distinct head. As the system matured enhanced melting and evaporation cooling rates spread farther to the rear of the storm, forming a large "mound-shaped" cold anomaly. Cooling by sublimation was found at the base of the stratiform cloud, just above the melting level, throughout. It will be shown that changes in the elements of particular microphysics schemes act to vary these sublimation, evaporation, and melting rates, and the manner in which they shift to the rear of the storm.

The Advanced Research Weather Research and Forecasting (WRF-ARW) model, version 3.2, was used to simulate an isolated bow echo case over Oklahoma on 13 March 2003. The simulations were performed with the WRF Single-Moment and Double-Moment 5- and 6-class schemes (WSM5, WSM6,

---

*Corresponding author address: Rebecca Adams-Selin, 16th Weather Squadron, HQ AFWA, 101 Nelson Dr. Offutt AFB, NE 68113; rebecca.selin.ctr@offutt.af.mil

WDM5, WDM6). Graupel distribution parameters within the WSM6 scheme, the intercept parameter and the density, were varied to make the graupel class more "graupel-like" or "hail-like". Additional comparisons were made between a WDM 5-class run, without a graupel class, and a WDM 6-class run. Almost every simulation produced a bowed line of convection, with bowing initiation similar to the real-data case. However, differences in the development and intensity of the cold pool, convective line, and stratiform rain region, system propagation speed, and new bowing development were all caused by these microphysical changes.

2. MODEL DESCRIPTION AND SETUP

2.1 Model design

The WRF-ARW model is widely recognized as a reliable model for real-data simulations of mesoscale phenomena. Here, version 3.2 is used. The initial conditions were provided by the National Center for Environmental Prediction (NCEP) Final Operational Global Analysis data, at 1° by 1° horizontal and six-hour temporal resolution. The model was initialized at 1200 UTC on 12 March 2003, and run for 36 hours to 0000 UTC 14 March 2003. A horizontal resolution of 3 km was used with 35 vertical levels; the domain is shown in Fig. 1. Parameterization schemes other than microphysics include the Mellor-Yamada-Janjic boundary layer scheme (Janjic 1994), the Noah land surface model, Rapid Radiative Transfer Model longwave radiation scheme, Goddard shortwave radiation scheme, and explicit convection (no convective parameterization). This combination, in addition to the set of microphysics schemes, was chosen after considerable experimentation as they produced the most realistic convective systems as compared to observations.
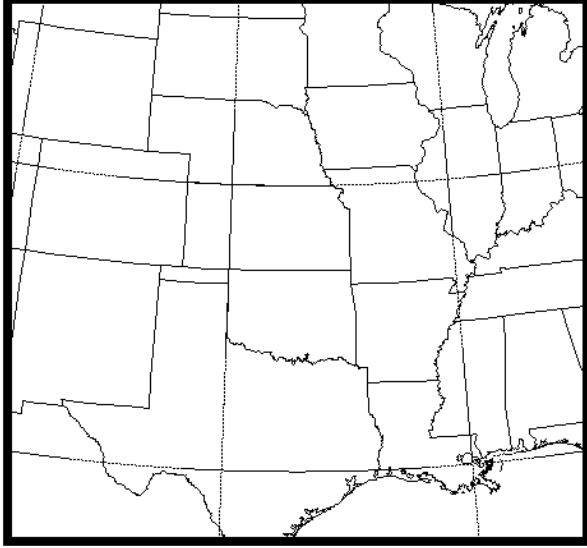
Figure 1: WRF-ARW domain. The entire domain was run in 3-km resolution. Later figures will show only a subsection of the domain over eastern Oklahoma for space considerations.

2.2 Model microphysics

The WRF Single-Moment and Double-Moment 5- and 6-class microphysics schemes (Hong et al. 2004; Hong and Lim 2006; Lim and Hong 2010) were originally based upon the techniques used in Lin et al. (1983) and Rutledge and Hobbs (1983). The 5-class schemes contain explicit classes for water vapor, cloud water, raindrops, cloud ice, and snow; the 6-class schemes add graupel. All of these schemes utilize an inverse exponential size distribution for snowflakes and (for the 6-class) graupel:

$$n_x(D_x)dD_x = n_{0x}exp(-\lambda_x D_x)dD_x \qquad (1)$$

where x is the microphysics class, D is diameter, n_{0x} is the distribution intercept, and λ_x is the slope. The distribution intercept is set to a constant value prior to processing. This is true even for the double-moment schemes as they only explicitly calculate a second moment (concentration) for the raindrop and cloud water distributions. The slope is a diagnosed value, defined as:

$$\lambda_x = (\frac{\pi \rho_x n_{0x}}{\rho q_x})^{0.25} \qquad (2)$$

where ρ_x is the pre-assigned particle density, ρ is the local air density, and q is the prognostic particle mixing ratio.

Table 1: Names of model simulations with the intercept value (n_{0G}) and density (ρ_G) is used. These range from the simulation with the most "hail-like" graupel class (n2d9) to the most "graupel-like" (n6d3). The default values in WSM6 are the settings for n6d5.

Simulation name	n_{0G} m^{-4}	ρ_G kg m^{-3}
n2d9	$4x10^2$	900
n4d9	$4x10^4$	900
n4d7	$4x10^4$	700
n6d5	$4x10^6$	500
n6d3	$4x10^6$	300

From (1), it can be seen that the size distribution of a particle is a function of the intercept, n_{0x}, and the slope, λ_x, which is a function of the particle density. As per Gilmore et al. (2004), previous observations of the intercept value for hail and graupel ranged from 10^2 m^{-4} for large hail, to 10^{10} m^{-4} for extremely small graupel (Cheng et al. 1985, Dennis et al. 1971; Federer and Waldvogel 1975; Spahn 1976; Knight et al. 1982). Observations of graupel density ranged from 50 to 890 kg m^{-3}; hail density varied from 700 to 900 kg m^{-3} (Pruppacher and Klett 1978). In the first portion of this experiment, model runs were designed to cover this range of variables, as shown in Table 1. The most "hail-like" particle, in model run n2d9, had an intercept equal to $4x10^2$ m^{-4} and a density of 900 kg m^{-3}. The most "graupel-like" particle, in run n6d3, had an intercept equal to $4x10^6$ m^{-4} and a density of 300 kg m^{-3}.

A plot of the graupel particle size distributions given the chosen intercepts and densities is shown in Fig. 2. It is evident that a decrease in the particle intercept yields an overall increase in the number of large particles while decreasing the number of small particles. This change in mean particle size will increase the mean terminal velocity. This will result in less dwell time in the downdraft, and therefore less time for melting and evaporation. Larger particles also have less surface area-to-volume ratio, which further reduces the melting and evaporation rates (van den Heever and Cotton 2004). A change in density alone has a much smaller effect. It will act to slightly decrease the number of very large particles, thereby also decreasing the mean terminal velocity.

Another set of simulations using the same initial values were run using the WRF Double-Moment 5- and 6-class schemes. Similar results were obtained with those runs, with one notable exception. The simulated reflectivity in the single-moment simulations was less intense than observed in the convective
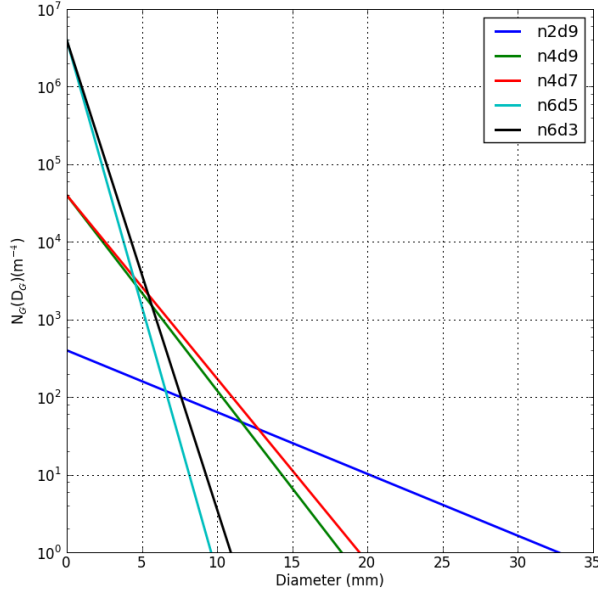
Figure 2: Graupel particle size distributions for the model runs given in Table 1.

Figure 3: 0600 UTC (a) and 0800 UTC (b) 13 March 2003 WSI NOWrad composite reflectivity data.

line. This deficiency is noted throughout each simulation, and the WRF double-moment schemes did not have such a problem. However WDM5 and 6 instead produced too intense stratiform precipitation. Examination of the differences between the single- and double-moment schemes will be reserved for a later study. For this experiment, the WSM schemes were chosen due to their reduced complexity, allowing for a more straightforward comparison. Simulations using the WDM schemes are shown in the next experiment, so it can be seen there are minor differences.

Finally, a set of simulations in which the WDM 5- and 6-class schemes were used to examine the importance of graupel as a class in simulating this type of convective system. WDM6 was run with the default graupel parameters (as in n6d5 in Table 1).

3. CASE REVIEW

Convection first initiated at 0215 UTC in north-central Oklahoma, and a convective line aligned southwest to northeast approximately 250 km in length formed by 0315 UTC (not shown). The system moved to the southeast at a speed of approximately 11 m s^{-1}. A trailing stratiform precipitation region appeared at 0500 UTC (not shown), and began to develop rearward. At 0600 UTC (Fig. 3.a) the center of the convective line bowed out; stratiform precipitation filled in behind the line as it bowed. A
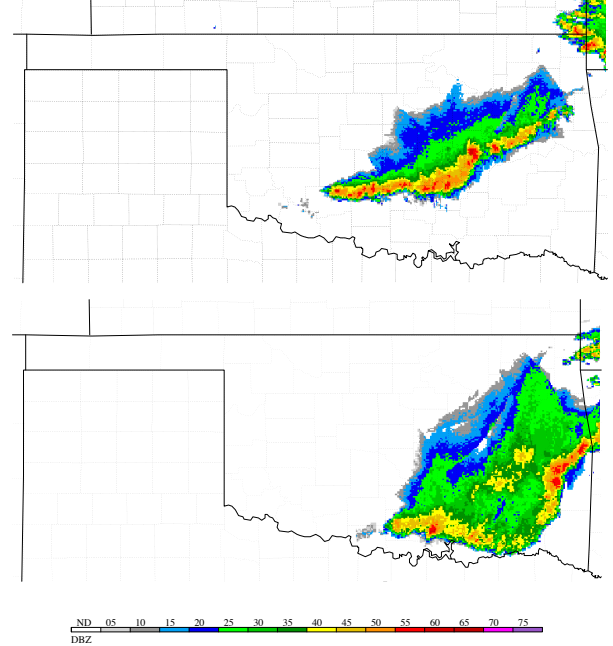
secondary reflectivity maximum formed in the stratiform region at 0700 UTC (not shown). The bow echo continued to increase in size until 0800 UTC (Fig. 3.b). At this point the convective line started to dissipate. The gust front associated with the decaying convective line, and the stratiform precipitation, continued to propagate southeastward over the next four hours. This eventually reformed into another mesoscale convective system in Louisiana (not shown).

4. RESULTS

4.1 Change in graupel/hail parameters

The spectrum of results between the "hail-like" n2d9 simulation and the "graupel-like" n6d3 simulation can be summarized by comparing the n2d9 and n6d3 runs. Both n2d9 and n6d3 initiated convection somewhat differently than observed: an isolated convective cell developed in southwestern Oklahoma at 0300 UTC (not shown) and moved southeast. By 0600 UTC, the convection in run n2d9 was cellular and appeared disorganized (Fig. 4a); a bow-shaped convective line formed in south-central Oklahoma in run n6d3 (Fig. 4b). (Note - the linear convection to the northeast of the initial system will not be considered here as it has no correspondence to observations.) As the n2d9 simulation progressed,
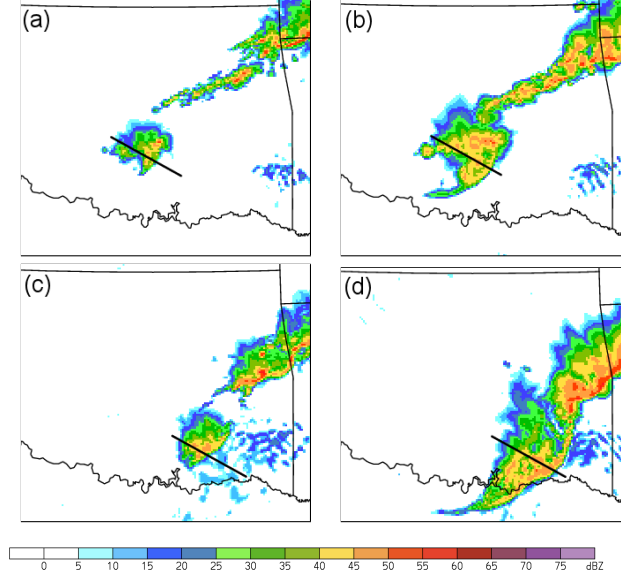
Figure 4: Simulated composite reflectivity data from WRF model simulation n2d9 (a, c) and n6d3 (b, d). 0600 (a, b) and 0800 (c, d) UTC 13 March 2003. Simulated reflectivity calculated as in Stoelinga (2005). Thick black lines delineate from where cross-sections will be shown in later figures.

it was simply unable to reproduce any of the typical features of a bow echo, particularly any sort of convective line (0800 UTC, Fig. 4c). The n2d9 system has less overall precipitation, both in intensity and area, than the n6d3 system. The system speed was also slower. At the same time the n6d3 simulation had further developed its bow shape as well as a stratiform precipitation region (Fig. 4d). Both systems began to dissipate at 0900 UTC, somewhat later than observations (not shown). However, the n6d3 system still appeared more organized, retaining its bow shape and some convective intensity while dissipating.

Figures 5 and 6 show cross-sections of each storm system taken across the convective line at 0600 UTC (see thick black lines in Fig. 4a,b for exact placement). In n2d9 (Fig. 5a), cloud ice and water, typically found in the updraft, and hail, typically found in the downdraft, are very close together. From this one can surmise the hail particles are too large to be sustained aloft in the convective updraft and fall out of the n2d9 system almost immediately upon formation. The convective updraft in the n2d9 simulation, which is almost entirely above 500 hPa (not shown), is nevertheless very upright and strong. This is likely due to the large concentration of condensation, freezing, and deposition processes immediately within and next to the updraft. From Fig. 6a, it is

evident that the large hail particles are so large, and fall so quickly, that they do not begin melting until almost reaching the surface. There is limited cooling by evaporation of raindrops. As a result, the n2d9 simulation cold pool is very shallow, and of weaker intensity (Fig. 5a). All cooling in the n2d9 simulation at this time is concentrated almost immediately behind the convective line; the cold pool is very narrow as well. Due to the weaker intensity, there is a gentle upward slope of potential temperature contours at the front of the n2d9 system (Fig. 5a), which reduces the intensity of the low-level updraft. Additionally, it is known the buoyancy gradient in the system with respect to height can be related to the associated pressure perturbation through

$$\frac{1}{\rho_0}\nabla^2 p' = -\nabla \cdot (\vec{v} \cdot \nabla \vec{v}) + \frac{\partial B}{\partial z} \qquad (3)$$

where p' is the perturbation pressure, $\vec{v}$ is the horizontal wind vector, and B is buoyancy, defined as $g\theta'_v/\bar{\theta}_v$. The buoyancy gradient is typically positive, due to the warmer updraft overlying the cold pool. In case n2d9, this gradient is still positive, but smaller, due to the warmer cold pool. Thus, (3) yields a positive but small $\nabla^2 p'$, and therefore a less intense mid-level low pressure perturbation (not shown). This further reduces the intensity of the low-level convective updraft, and also helps the updraft remain more upright instead of titled (not shown).

In the n6d3 system, precipitation is advected rearward farther from the convective line, as evidenced by the larger, 70-km wide stratiform region (Fig. 5b). There are large concentrations of graupel and snow both closer to the convective line and farther behind the system. Because of the smaller nature of the graupel particles, they are more easily held aloft and advected rearward. From Fig. 6b, high rates of deposition, melting, and evaporation of the falling graupel and snow out of the stratiform precipitation region are evident. Due to the smaller size of these particles, they undergo sublimation, melting, and evaporation quickly; the small particles melt almost immediately once falling below the melting level. These processes are also enhanced by the longer dwell time aloft due to the slower fall speeds. Therefore the cooling rates in n6d3 are much larger, and also are spread over a much larger area than the n2d9 run. The heightened cooling rates result in a more intense, deeper, and larger cold pool (Fig. 5b), as discussed earlier. Specifically, the cold pool in n6d3 is 4 K colder than the n2d9 cold pool, and almost 70 km wider and 30 hPa deeper. The
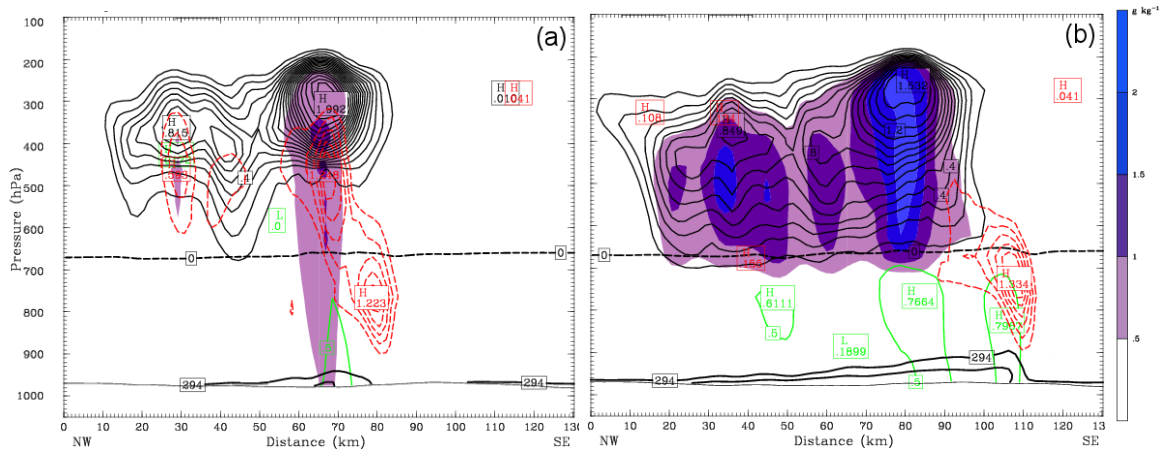
Figure 5: Model output from n2d9 simulation (a) and n6d3 simulation (b) at 0600 UTC 13 March 2003. The cross-section is taken along the black lines in Figs. 4a, b; plotted values are averages of 15 km either side of the cross-section. Mixing ratios (g kg^{-1}) are of graupel (image), cloud water and ice (dashed red, 0.2 g kg^{-1}), rain water (green, 0.5 g kg^{-1}), and snow (thin black, 0.1 g kg^{-1}) are in (g), (h); the thick black lines are cold pool potential temperature contours (2 K) at 294 K and colder. Thick dashed black line is the melting level.
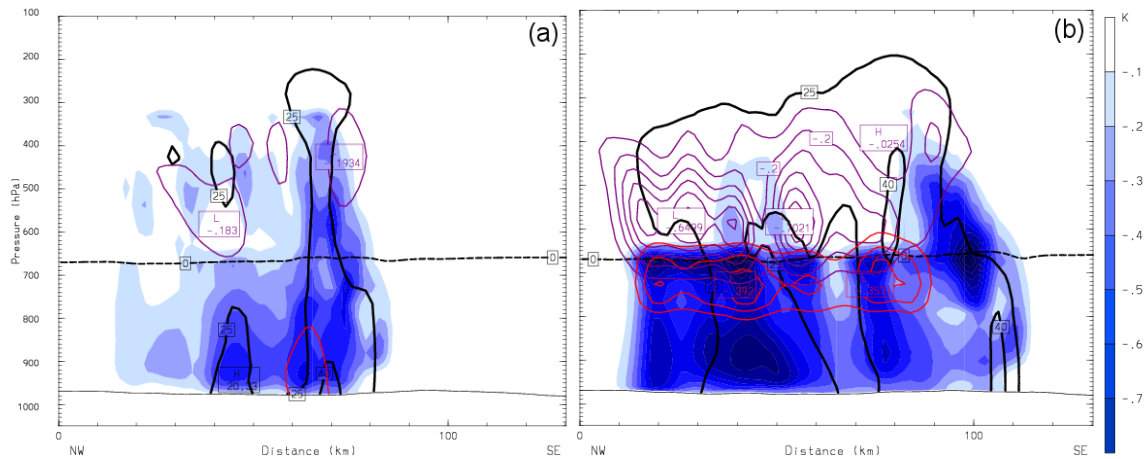

Figure 6: As in Fig. 5, except with cooling rates (K (5 min)$^{-1}$) by evaporation (blue image), melting (red, 0.1 K (5 min)$^{-1}$), and sublimation (purple, 0.1 K (5 min)$^{-1}$). Thick solid black line is the simulated reflectivity at 25, 40, and 50 dBZ. Thick dashed black line is the melting level.

convective updraft is also tilted more over the cold pool (not shown). Because hydrometeor particles are being advected farther rearward, freezing and deposition rates are higher across the upper levels of the stratiform region. The latent heat released by these processes helps create a stronger and larger stratiform updraft. Additionally, the wider, colder cold pool allows for a stronger buoyancy gradient with respect to height, decreasing the mid-level low pressure gradient, further helping increase the convective updraft intensity and tilt. Downdrafts are also almost entirely confined to the stratiform precipitation region (not shown). Finally, gravity current theory suggests a more intense cold pool will result in a faster-moving convective system; this is indeed the case.

Fig. 7 shows cross-sections of the two simulations at 0800 UTC. In the n2d9 simulation, the hail and rain has begun falling into the updraft (Fig. 7a). The system appears similar to a dying pulse-type thunderstorm. The cold pool is still minimal. Its deepest part has shifted slightly rearward of the convective line, but peak cooling rates (not shown) still remain much closer to it than as in n6d3. In n6d3, the stratiform region is still significantly larger than in n2d9; the cold pool is as well (Fig. 7b). However, peak cooling rates have shifted farther rearward into the area below the middle of the stratiform region (not shown). The deepest part of the cold pool is approximately 50 km behind the convective line. Meanwhile the mid-level low pressure perturbation associated with this system has grown stronger but shifted rearward (not shown). As a result the low-level convective updraft is tilted even more rearward over the cold pool. This proves to be too extreme of a tilt, as the system begins dissipating shortly after this by 0900 UTC.

4.2 *Removal of graupel class*

The WRF Double-Moment 5-class and 6-class schemes are identical, except for the inclusion of graupel as a class in the 6-class scheme (Lim and Hong 2010). Simulations using both the 5- and 6-class schemes were run to examine the importance of graupel as a class, as hinted at in the above hail/graupel comparisons. Figure 8 shows the simulated model reflectivity for these two runs. During initiation (0445 UTC), the 5-class scheme simulation (WDM5) generated unrealistically large stratiform regions both in advance of and behind the still developing convective line (Fig. 8a). This was due to the widespread concentrations of slowly falling snow crystals in the upper levels (Fig. 9a). At this

time, the WDM5 stratiform precipitation remained entirely aloft, with melting and evaporative cooling beneath it. This cooling was likely balanced by subsidence drying as the air descended, resulting in an almost non-existent cold pool (Fig. 9a). At 0530 UTC, precipitation reached the ground (not shown), and the convective line continued to develop and was fully in place by 0600 UTC (Figs. 8b, 9b). The atmospheric layers beneath the stratiform region were saturated as the system reached maturity, and the stratiform precipitation region extended completely to the surface (Fig. 9b). While there were more, smaller snow crystals to melt and evaporate, theoretically leading to a colder cold pool, these saturated layers did not allow evaporation to take place. Thus, the cold pool in the WDM5 simulation was significantly shallower and warmer than in the WDM6 simulation, as will be seen later. By 0730 UTC, however, the WDM5 simulation gained convective intensity and began bowing (Fig. 8c). The system was well organized, with a tightly defined convective line and less intense but extensive stratiform region that was entirely rearward of the convective line. There was additionally a secondary maximum of reflectivity in the stratiform region, separated from the convective line by a transition zone, which matches observations well. Furthermore, the area beneath the stratiform rain region was no longer saturated by this time (Fig. 9c) allowing for a more developed cold pool. Yet, because the cold pool was initially warmer, the WDM5 system moved relatively slowly. Possibly this speed, and the resulting storm-relative environmental wind shear, was optimal as it allowed the relative vorticities generated by the cold pool and environmental wind shear to balance each other well. The overall system became more intense as time progressed and a more organized and life-like system was created. At 0900 UTC, the system began to dissipate, although the convective line was still fairly intense (greater than 45 dBZ, not shown).

The system in the WDM6 simulation developed intense convection by 0445 UTC (Fig. 8d). At this point the convection was cellular, with minimal stratiform precipitation. The larger graupel hydrometeors were not as mobile, and stayed closer to the convective updraft. (Fig. 10a). The cold pool was still very minimal at this point, but was larger than the corresponding time in the WDM5 simulation. Cooling rates due to melting graupel, and evaporating rain/melted graupel, were approximately equal at this point (not shown); the subcloud layer was subsaturated. By 0600 UTC, the system developed mature mesoscale convective system features, such as a convective line and intense
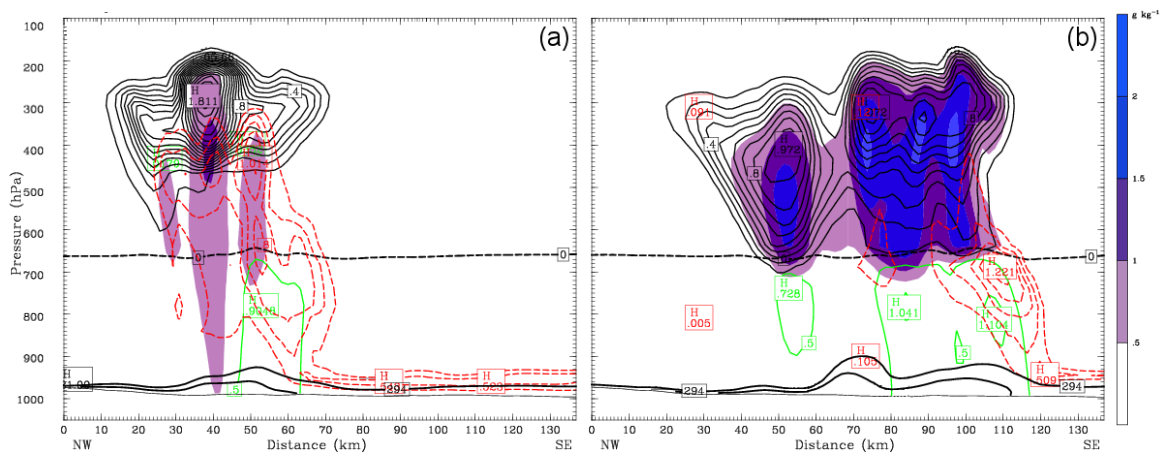
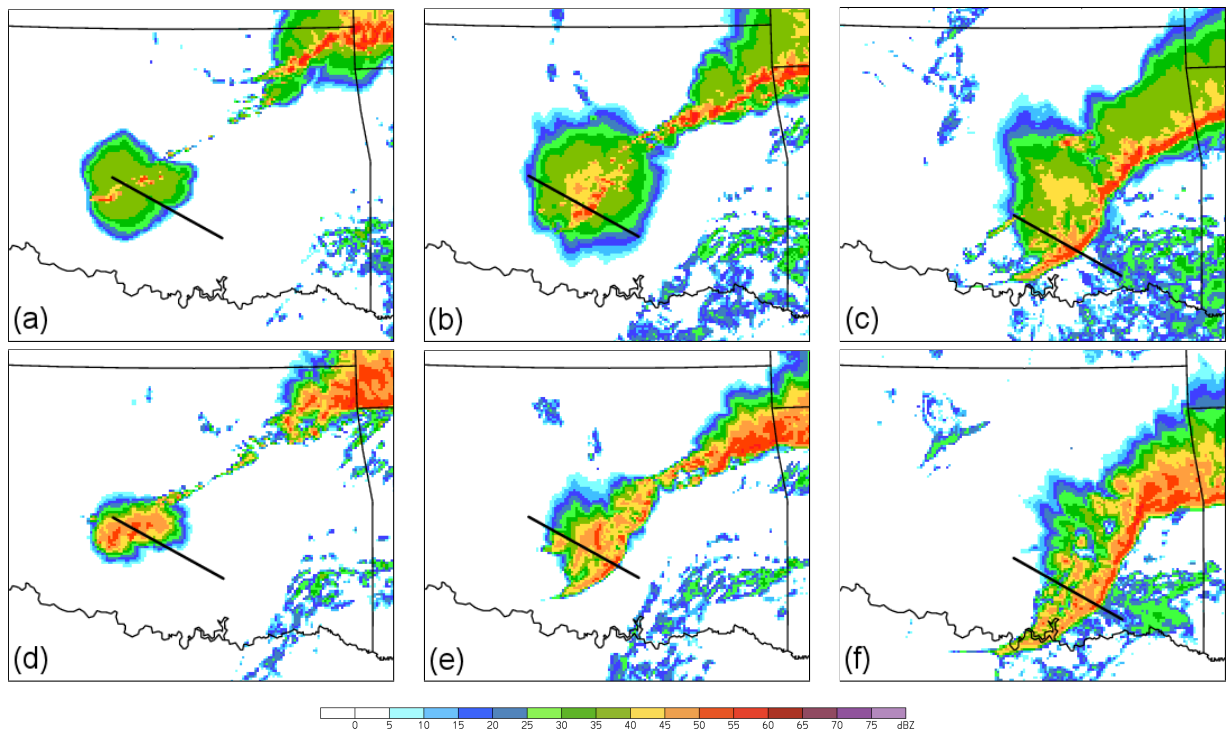Figure 7: As in Fig. 5, but for 0800 UTC. New cross-section location is given in Fig. 4c, d.

Figure 8: Simulated composite reflectivity data from WRF model simulation WDM5 (a,b,c) and WDM6 (d,e,f). Columns, from left to right, correspond to times 0445 (a, d), 0600 (b, e), and 0730 (c, f) UTC 13 March 2003. Simulated reflectivity calculated as in Stoelinga (2005). Thick black lines delineate from where cross-sections will be shown in later figures.

stratiform precipitation region (Fig. 8e). Large concentrations of graupel and snow aloft composed the stratiform region, but these concentrations were not as large, both in quantity and area, as the snow concentrations in the WDM5 run at the same time (Fig. 10b). The cold pool, cooled by both melting and evaporating graupel and evaporating rain falling through a still sub-saturated sub-cloud layer, was much larger, deeper, and cooler than the WDM5 system (6 K cooler at its most intense point; Fig. 10b). The cold pool at this point also had a distinct head, as the cooling maximum in the WDM6 system was closer to the convective line due to the graupel not spreading as far from the updraft. As of 0730 UTC, the stratiform precipitation area had become much less organized (Fig. 8f), with diminished amounts of snow and graupel particles aloft (Fig. 10c). Examination of vertical wind speeds revealed that the low-level convective updraft, at the front edge of the cold pool, had moved more quickly than the upper-level updraft associated with the stratiform region (not shown). By this point, the disparate speeds forced the disorganization of the system. The cold pool developed a mound shape with the deepest point beneath the stratiform precipitation region, as the main source of cooling shifted to beneath the stratiform region (Fig. 10c). The mid-level low pressure perturbation had also intensified, further helping to tilt the updraft (not shown). At 0730 UTC, the WDM6 system remained intense, but was disorganized; after 0800 UTC the system lost its convective line and began to slowly dissipate.

5. CONCLUSIONS

Simulations were performed over a spectrum of graupel class parameters, rendering the class more dense and "hail-like", or lighter and "graupel-like". Additional simulations looked at the effects of removing graupel completely.

The simulations with a larger, more dense "hail-like" graupel class had these particles fall out of the updraft almost immediately, close to the convective line, allowing little melting or evaporation. This resulted in a minimal stratiform precipitation region and weaker cold pool. Because of this, there were fewer feedbacks to updraft intensity, such as a weaker mid-level low pressure perturbation. There was little convection and no bowing. Meanwhile, the simulations with a smaller, less dense "graupel-like" graupel class had a mixture of small snow crystals and larger graupel particles that were slower to fall, creating a wide stratiform precipitation region. This allowed for more melting and evaporation, and

yielded a wider, deeper, and colder cold pool. The mid-level low pressure perturbation associated with the system was stronger, strengthening the low-level convective updraft. Also, the cold pool retained its "head" shape longer.

The WDM5 simulation without graupel formed entirely aloft, as the numerous small snowflakes generated fell very slowly. The system developed downward toward the surface, and the stratiform precipitation region only reached the surface as the system became vertically saturated. This saturation allowed for little evaporation; hence the system was slower and initially not as intense as the WDM6 simulation with graupel. However, this slower speed allowed the system to remain more organized, with its convective and stratiform updrafts staying closer together. Over time this simulation developed a very distinct leading convective line, and had a less intense but more realistic stratiform region, and a slightly more intense bow echo. The WDM6 simulation with graupel initially developed a stronger cold pool, as its sub-cloud layer was not saturated. However, the fast speed of the system, coupled with the stronger mid-level lower pressure gradient, helped tilt the updraft too far over the cold pool. This system became disorganized more quickly, approximately an hour earlier than the WDM5 simulation.

Thus, it was found that internal variations in the WRF Single- and Double-Moment microphysics schemes, specifically regarding the graupel class, had a large effect on the structure, strength, and longevity of the simulated convective system. As there are many environmental factors that could result in similar microphysical changes, such as variations in nearby temperature, moisture, shear, or aerosol profiles, these results are of note. Future work includes using WSR-88D radar data to more fully compare the model simulations to observations. Idealized simulations will be performed to further isolate the effects of changing microphysical parameters on a typical bow echo system.

7. REFERENCES

Cheng, L. M. English, and R. Wong, 1985: Hailstone size distributions and their relationship to storm thermodynamics. *J. Climate App. Meteor.*, **24**, 1059–1067.

Dennis, A. S. P. L. Smith Jr. G. A. P. Peterson, and R. D. McNeil, 1971: Hailstone size distributions and equivalent radar reflectivity factors computed from hailstone momentum records. *J. App. Meteor.*, **10**, 79–85.

Dawson, D. T. II, M. Xue, and J. A. Milbrandt, 2008: Improvements in the treatment of evaporation and melting in multi-moment versus single-moment bulk microphysics: Results from numerical simulations of the 3 May 1999 Oklahoma tornadic storms. *24th Conf. on Severe Local Storms*, Savannah, Georgia, Amer. Meteor. Soc. 17B.4.

Dawson, D. T. II, M. Xue, J. A. Milbrandt, M. K. Yau, and G. Zhang, 2007: Impact of multi-moment microphysics and model resolution on predicted cold pool and reflectivity intensity and structures in the Oklahoma tornadic supercell storms of 3 May 1999. *22nd Conf. Wea. Anal. Forecasting/18th Conf. Num. Wea. Pred.*, Salt Lake City, Utah, Amer. Meteor. Soc. CD-ROM 10B.2.

Federer, B. and A. Waldvogel, 1975: Hail and raindrop size distributions from a Swiss multicell storm. *J. App. Meteor.*, **14**, 91–97.

Gallus, W. A. Jr. and R. H. Johnson, 1995: The dynamics of circulations within the trailing stratiform regions of squall lines: Part I: The 10-11 June PRE-STORM system. *J. Atmos. Sci.*, **52**, 2161–2187.

Gilmore, M. S. J. M. Straka, and E. N. Rasmussen, 2004: Precipitation uncertainty due to variations in precipitation particle parameters within a simple microphysics scheme. *Mon. Wea. Rev.*, **132**, 2610–2627.

Hong, S.Y. J. Dudhia, S.H. Chen, 2004: A revised approach to ice microphysical processes for the bulk parameterization of clouds and precipitation. *Mon. Wea. Rev.*, **132**, 103–120.

Hong, S.Y. and J.O. J. Lim, 2006: The WRF single-moment 6-class microphysics scheme (WSM6). *J. Korean. Meteor. Soc.*, **42**, 129–151.

Janjic, Z. 1994: The step-mountain eta coordinate model: Further developments of the convection, viscous sublayer, and turbulence closure schemes. *Mon. Wea. Rev.*, **122**, 927–945.

Knight, C. A. W. A. Cooper, D. W. Breed, I. R. Paluch, P. L. Smith, and G. Valie, 1982: Microphysics. *Hailstorms of the Central High Plains*, C. Knight and P. Squires, Eds. Vol. 1, Colorado Associated University Press, 151–193.

Lim, K.S. S. and S.Y. Hong, 2010: Development of an effective double-moment cloud microphysics scheme with prognostic cloud condensation nuclei (CCN) for weather and climate models. *Mon. Wea. Rev.*, **138**, 1587–1612.

Lin, Y.L. R. D. Farley, and H. D. Orville, 1983: Bulk parameterization of the snow field in a cloud model. *J. Climate App. Meteor.*, **22**, 1065–1092.

Pruppacher, H. R. and J. D. Klett, 1978: *Microphysics of Clouds and Precipitation*. D. Reidel, 714 pp.

Rutledge, S. A. and P. V. Hobbs, 1983: The mesoscale and microscale structure and organization of clouds and precipitation in mid-latitude cyclones. Part VIII: A model for the "seeder feeder" process in warm-frontal rainbands. *J. Atmos. Sci.*, **40**, 1185–1206.

Snook, N. A. and M. Xue, 2006: Sensitivity of tornadogenesis in very-high resolution numerical simulations to variations in model microphysical parameters. *23 Conf. on Severe Local Storms*, St. Louis, Missouri, Amer. Meteor. Soc. 16.4.

Spahn, J. E. 1976: The airborne hail disdrometer: An analysis of its 1975 performance. Rep. 76-13, Institute of Atmospheric Sciences, South Dakota School of Mines and Technology, Rapid City, SD, 65 pp.

Stoelinga, M. T. 2005: Simulated equivalent reflectivity factor as currently formulated in RIP: Description and possible improvements, Read/Interpolate/Plot implementation document.

van den Heever, S. C. and W. R. Cotton, 2004: The impact of hail size on simulated supercell storms. *J. Atmos. Sci.*, **61**, 1596–1609.

Weisman, M. L, 1993: The genesis of severe long-lived bow echoes. *J. Atmos. Sci.*, **50**, 645–670.

Weisman, M. L. 1992: The role of convectively generated rear-inflow jets in the evolution of long-lived meso-convective systems. *J. Atmos. Sci.*, **49**, 1826–1847.
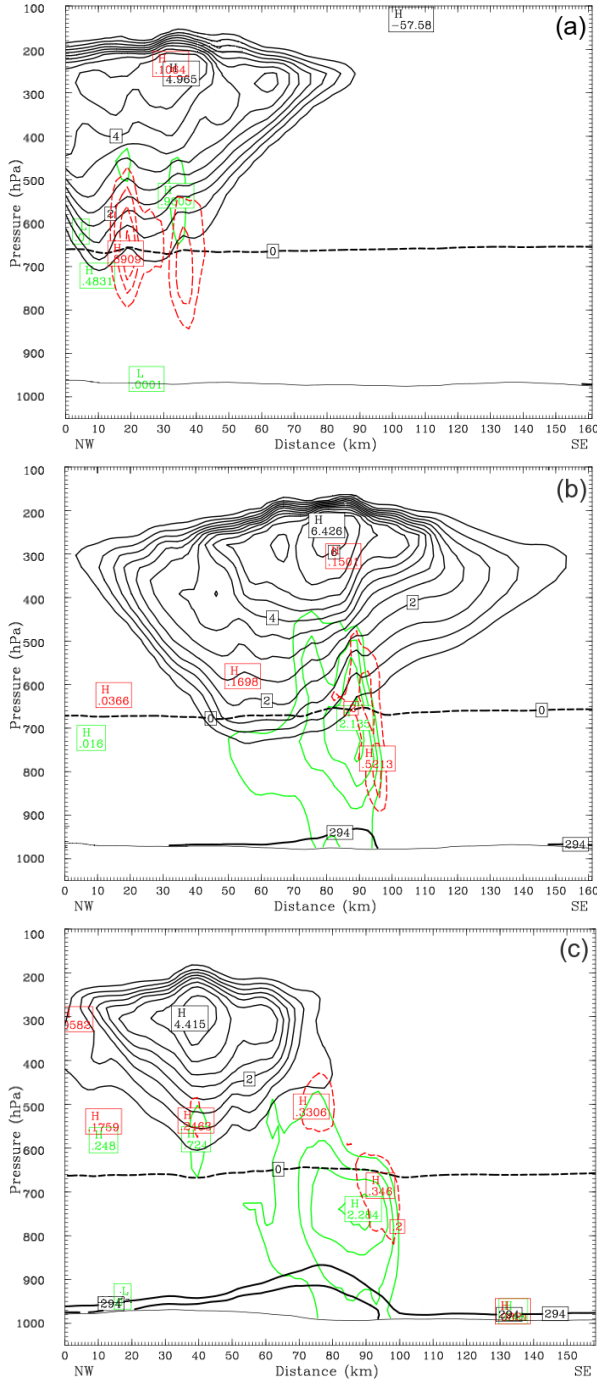
Figure 9: Mixing ratio cross-section from the WDM5 simulation, at 0445 (a), 0600 (b), and 0730 (c) UTC 13 March 2003 from cross-section lines shown in Fig. 8. Values are averages of 15 km either side of cross-section. Mixing ratios $(\mathrm{g\,kg^{-1}})$ are of cloud water and ice (dashed red, $0.2\ \mathrm{g\,kg^{-1}}$), rain water (green, $0.5\ \mathrm{g\,kg^{-1}}$), and snow (thin black, $0.5\ \mathrm{g\,kg^{-1}}$). The thick black lines are cold pool potential temperature contours (2 K) at 294 K and colder. The thick dashed black line is the melting level.
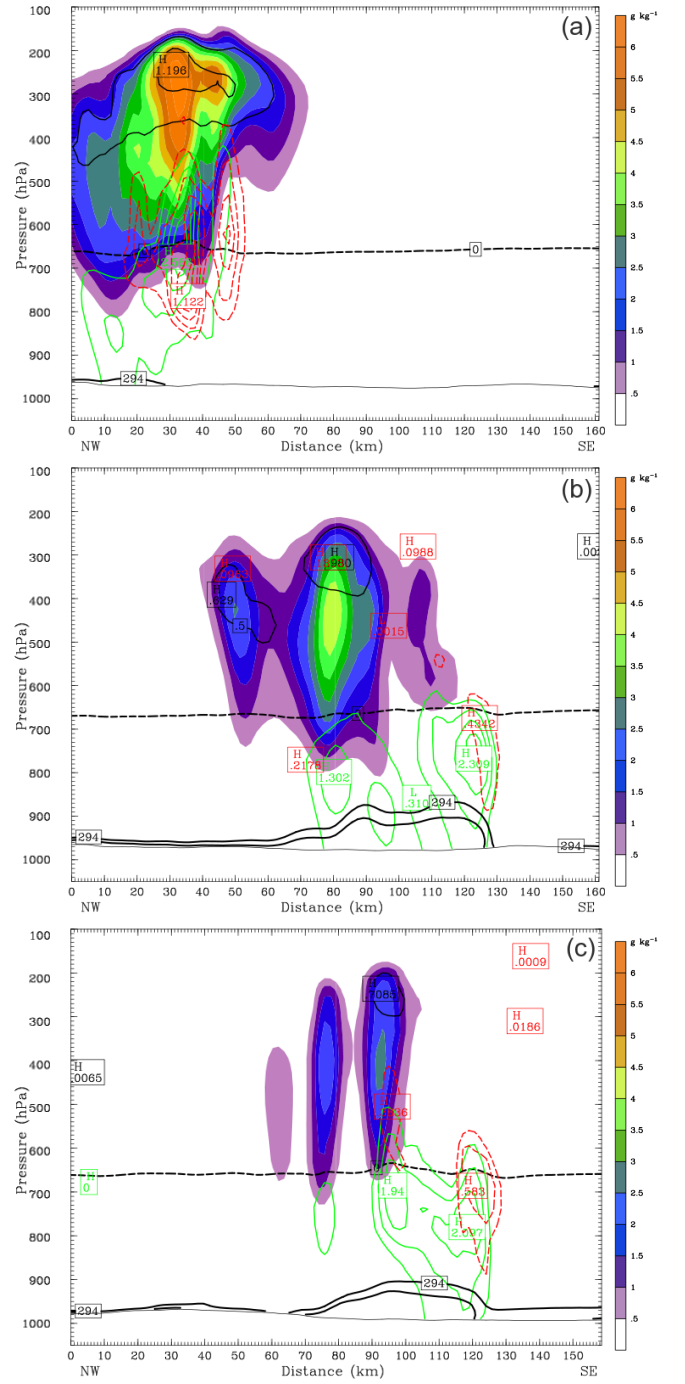
Figure 10: As in Fig. 9, but for the WDM6 simulation.